

Article

Formation and Stability of Interface between Garnet-Type Ta-doped Li₇La₃Zr₂O₁₂ Solid Electrolyte and Lithium Metal Electrode

Ryoji Inada * , Satoshi Yasuda, Hiromasa Hosokawa, Masaya Saito, Tomohiro Tojo  and Yoji Sakurai

Department of Electrical and Electronic Engineering, Toyohashi University of Technology, 1-1 Tempaku-cho, Toyohashi, Aichi 4418580, Japan; yasuda@cec.ee.tut.ac.jp (S.Y.); hosokawa@cec.ee.tut.ac.jp (H.H.); saito@cec.ee.tut.ac.jp (M.S.); tojo@ee.tut.ac.jp (T.T.); sakurai@ee.tut.ac.jp (Y.S.)

* Correspondence: inada@ee.tut.ac.jp; Tel.: +81-532-44-6723

Received: 10 May 2018; Accepted: 6 June 2018; Published: 7 June 2018



Abstract: Garnet-type Li_{7-x}La₃Zr_{2-x}Ta_xO₁₂ (LLZT) is considered a good candidate for the solid electrolyte in all-solid-state lithium batteries because of its reasonably high conductivity around 10^{-3} S cm⁻¹ at room temperature and stability against lithium (Li) metal with the lowest redox potential. In this study, we synthesized LLZT with a tantalum (Ta) content of 0.45 via a conventional solid-state reaction process and constructed a Li/LLZT/Li symmetric cell by attaching Li metal foils on the polished top and bottom surfaces of an LLZT pellet. We investigated the influence of heating temperatures and times on the interfacial charge-transfer resistance between LLZT and the Li metal electrode. In addition, the effect of the interface resistance on the stability for Li deposition and dissolution was examined using a galvanostatic cycling test. The lowest interfacial resistance of $25\ \Omega\text{cm}^2$ at room temperature was obtained by heating at $175\ ^\circ\text{C}$ ($5\ ^\circ\text{C}$ lower than the melting point of Li) for three to five hours. We confirmed that the current density at which the short circuit occurs in the Li/LLZT/Li cell via the propagation of Li dendrite into LLZT increases with decreasing interfacial charge transfer resistance.

Keywords: garnet; solid electrolyte; lithium metal; interface; charge-transfer resistance

1. Introduction

A high performance electrical energy storage device is a key technology in the sustainable development of a ubiquitous and clean energy society. Rechargeable lithium-ion batteries (LIBs), using graphite as the anode and organic liquid electrolyte and lithium transition-metal oxide as the cathode, were commercialized in 1991 and have since been widely used worldwide as a power source for mobile electronic devices, such as cell phones and laptop computers because of their high-energy density and reasonably good cycling performance. The development of middle- or large-scale LIBs has accelerated for use in automotive propulsion and stationary load-leveling for intermittent power generation from solar or wind energy [1–3]. However, a larger battery size creates more serious safety issues in LIBs; one of the main reasons for this being the increased amount of flammable organic liquid electrolytes.

All-solid-state lithium-ion batteries with a non-flammable inorganic Li⁺ ion conductor as a solid electrolyte (SE) are expected to be the next generation of energy storage devices because of their high energy density, safety, and excellent cycle stability [4–6]. The SE materials should possess not only high Li⁺ ion conductivity above one mS cm⁻¹ at a room temperature but also chemical stability against electrode materials, air, and moisture. Oxide-based SE materials have rather lower conductivity and poor plasticity compared with sulfide-based materials, but they have other advantages such as their chemical stability and ease of handling [7,8].

Garnet-type Li⁺ ion conducting oxide, Li₇La₃Zr₂O₁₂ (LLZ), has been widely investigated because of its good ionic conduction, excellent thermal performance, and wide electrochemical potential window [9]. LLZ has two different crystal phases: the cubic phase [9,10] and the tetragonal phase [11,12]. However, high conductivity above 10⁻⁴ S cm⁻¹ at a room temperature range is only obtained in the former, densified by high temperature sintering. Partial substitution of the Zr⁴⁺ site in LLZ by other higher valence cations, such as Nb⁵⁺ [13,14], Ta⁵⁺ [15–23], W⁶⁺ [24,25], and Mo⁶⁺ [26], is effective at stabilizing the cubic phase, and the conductivity at room temperature is greatly improved to 1 mS cm⁻¹ by controlling the dopants content and optimizing Li⁺ concentration in the garnet framework. Although a solid-state battery with an Nb-doped LLZ as SE has already been demonstrated [13,27,28], a Ta-doped LLZ showed much better chemical stability against a Li metal electrode than when Nb-doped [29,30]. The other dopants, such as W⁶⁺, Mo⁶⁺, or Nb⁵⁺ in LLZ, could potentially become a redox center at relatively high potential against Li⁺/Li [31].

The use of Li metal with extremely large gravimetric specific capacity (3860 mAh g⁻¹) with the lowest redox potential as an anode leads to the high energy density of a battery, but the formation of a solid-solid interface among garnet-type SE and Li metal electrodes is another challenging issue in achieving better electrochemical performance in solid-state batteries [32–34]. Many approaches have been introduced to reduce the interfacial charge-transfer resistance between garnet-type SE and Li, including the introduction of thin film layers of Au [35], Si [36], Ge [37], Al₂O₃ [38], and ZnO [39], or eliminating the secondary phases, such as LiOH and Li₂CO₃, by polishing the surface of SE and using multiple thermal treatments at specific temperatures before and after contact with Li [40–42]. However, a more simplified method to form the interface between garnet-type SE and the Li electrode would be preferable and further study is required of the relationship between the interfacial charge-transfer resistance and stability for Li deposition and dissolution reaction at the interface.

In this work, we synthesized a cubic garnet-type LLZT using a solid-state reaction process. An Li/LLZT/Li symmetric cell, created by attaching Li metal foil on the top and bottom surfaces of an LLZT pellet, was used to examine the influence of heating temperatures and times on the interfacial charge-transfer resistance between LLZT and Li. Moreover, the effect of the interface resistance on the stability of Li deposition and dissolution reactions at the Li/LLZT interface was systematically investigated using a galvanostatic cycling test.

2. Materials and Methods

2.1. Synthesis and Characterization of LLZT

LLZT with a Ta content (x) of 0.45 was synthesized using a conventional solid-state reaction process. Notably, we did not use an Al₂O₃ crucible for sample synthesis because Al³⁺ contamination from the crucible into the LLZT lattice during high temperature sintering may influence the Li⁺ contents and, generally, this contamination level cannot be precisely controlled. The following were obtained from the Kojundo Chemical Laboratory (Saitama, Japan): stoichiometric amounts of LiOH·H₂O (99% with 10% excess was added to account for the evaporation of lithium at high temperatures), La(OH)₃ (99.99%), ZrO₂ (98%) and Ta₂O₅ (99.9%), which were then ground and mixed by planetary ball-milling (Nagao System, Planet M2-3F, Kawasaki, Japan) with zirconia balls and ethanol for 3 h in a zirconia pot, and then calcined at 900 °C for 6 h in air using a Pt-5% Au alloy crucible. The calcined powders were ground again by planetary ball-milling for 1 h, and then pressed into pellets at 300 MPa by cold isostatic pressing. Finally, the pellets were sintered at 1150 °C for 15 h in air using a Pt-5% Au alloy crucible. To minimize Li loss and the formation of secondary phases during the sintering process, the pellets were covered with the same mother powder.

The crystal phase of LLZT was evaluated by X-ray diffraction (XRD; Rigaku Multiflex, Tokyo, Japan) using CuK α radiation ($\lambda = 0.15418$ nm), with a measurement range 2θ of 5–90° and a step interval of 0.004°. Scanning electron microscope (SEM) observation of the fractured surface microstructure of the sintered LLZT was performed using a scanning electron microscope (SU8000 Type II, HITACHI,

Tokyo, Japan).). The electrical conductivity of each LLZT was evaluated with alternating current (A/C) impedance measurements using a chemical impedance meter (3532-80, HIOKI, Ueda, Japan) at temperatures from 27 to 100 °C, frequencies from 5 Hz to 1 MHz, and an applied voltage amplitude of 0.1 V. Li⁺-blocking Au film electrodes were formed on both parallel surfaces of the pellet by sputtering for the conductivity measurement.

2.2. Evaluation of Stability for LLZT/Li Interface

To evaluate interface stability between LLZT and Li metal, we constructed the Li/LLZT/Li symmetric cell with a cell fixture (Figure 1) in an Ar-filled glove box by attaching Li metal foils on the polished top and bottom surfaces of an LLZT pellet with a thickness between 1.90 and 1.95 mm. Heat treatments at different temperatures (100–175 °C) and time (1–5 h) were applied to the cell after cell construction. Interfacial charge-transfer resistance $R_{\text{Li-LLZT}}$ between LLZT and Li was evaluated by A/C impedance measurements. The influence of $R_{\text{Li-LLZT}}$ on the stability of the Li deposition and dissolution reaction was also investigated using galvanostatic cycling testing of a symmetric cell at 25 °C using a Battery Test System (TOSCAT-3100, TOYO SYSTEM, Iwaki, Japan). The microstructure of the LLZT pellet after the galvanostatic testing was observed by SEM (SU8000 Type II, HITACHI, Tokyo, Japan).



Figure 1. Illustration (left) and photo of cell fixture for composing a lithium-garnet-type $\text{Li}_{7-x}\text{La}_3\text{Zr}_{2-x}\text{Ta}_x\text{O}_{12}$ -lithium (Li/LLZT/Li) symmetric cell.

3. Results and Discussion

3.1. Characterization of Sintered LLZT Pellets

The XRD pattern and SEM image of the fractured surface of sintered LLZT are shown in Figure 2. The calculated pattern with the reported structural parameters for cubic LLZ is also plotted in Figure 2a [7]. All the peaks for the LLZT sample were well indexed as cubic garnet-type structures with a space group $Ia\bar{3}d$; no other secondary phases were observed. Compared with the calculated pattern for cubic LLZ, all peaks of LLZT shifted toward a higher angle 2θ . This was attributed to the reduction in the lattice size by substitution of Zr⁴⁺ (72 pm) by smaller Ta⁵⁺ (64 pm) [15–23]. As shown in Figure 2b, the average grain size in the sintered LLZT was around 5 μm and all grains were in good contact with each other to form a dense structure. The density of the pellet was determined from their weight and physical dimensions. The relative density (measured density normalized by the theoretical density) of LLZT used in this work was around 92–93%.

The ionic conductivity of LLZT was examined by A/C impedance spectroscopy using a Li⁺ ion blocking silver (Au) electrode. Figure 3a shows the Nyquist plots of A/C impedance measured at 27, 50, and 75 °C for LLZT. A part of the small semicircle and linear portion data were obtained in high and low frequency regions, indicating that the conduction is primarily ionic in nature. The intercept point of the linear tail in the low frequency range with a real axis corresponds to the sum of the bulk and grain-boundary resistances. Total conductivity σ was calculated by the inverse of the total (bulk

and grain boundary) resistance and geometrical parameters of the pellet, which was estimated to be 0.93 mS cm^{-1} at 27°C . Notably, we prepared many LLZT pellets for stability testing described later, and all pellets reproducibly showed $\sigma = 0.9\text{--}1.0 \text{ mS cm}^{-1}$ at 27°C .

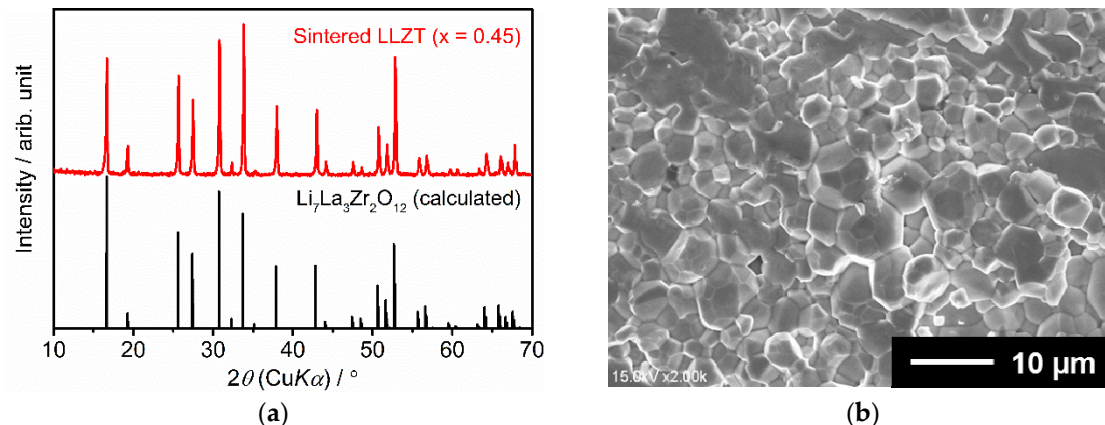


Figure 2. (a) X-ray diffraction (XRD) pattern and (b) scanning electron microscope (SEM) image of fractured cross section for sintered LLZT.

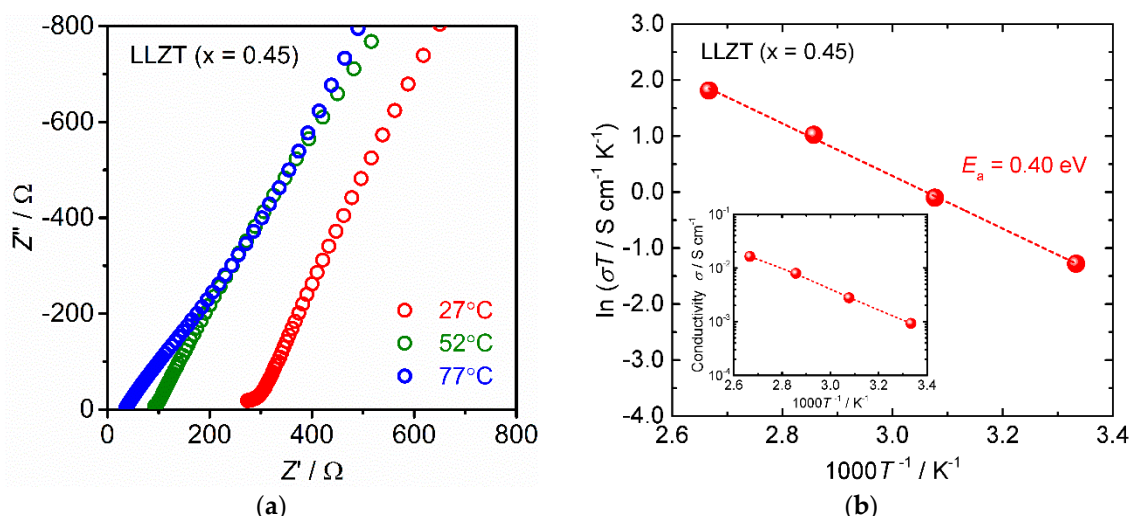


Figure 3. (a) Nyquist plot of alternating current (A/C) impedance of LLZT at 27°C . (b) Arrhenius plot of the conductivity σ for LLZT plotted against the inverse of measurement temperature.

Figure 3b shows the variation in σ for an LLZT pellet as a function of an inverse of temperature $1000 T^{-1}$. σ increased monotonically as the temperature increased and reached 16 mS cm^{-1} at 100°C . In addition, the temperature dependence of σ was well-expressed by the Arrhenius equation as $\sigma = \sigma_0 \exp(-E_a/(k_B T))$, where σ_0 is constant, E_a is the activation energy of conductivity, and k_B is the Boltzmann constant ($1.381 \times 10^{-23} \text{ J K}^{-1}$). From the slope data of σT in Figure 3b, E_a of LLZT was calculated as 0.40 eV , which is nearly the same as the Al-free LLZT reported in the literature [19,21,22].

3.2. Interfacial Charge Transfer Resistance between LLZT and Li Metal Electrode

To examine the effect of a heat treatment condition on $R_{\text{Li-LLZT}}$ between LLZT and Li, we measured the A/C impedance of Li/LLZT/Li symmetric cells with various heat treatment conditions. Figure 4a shows the Nyquist plots of A/C impedance at 27°C for Li/LLZT/Li cell both before and after heat treatment at different temperatures for one hour. The data in Figure 4a were obtained in a continuous

experiment with one specific cell. Firstly, we measured the impedance for the cell before applying heat treatment, then the cell was heat-treated at 100 °C for one hour, cooled down to 27 °C, and the impedance measurements were recorded. After that, measurements for the cell heat-treated at 150 or 175 °C for one hour were recorded in sequence.

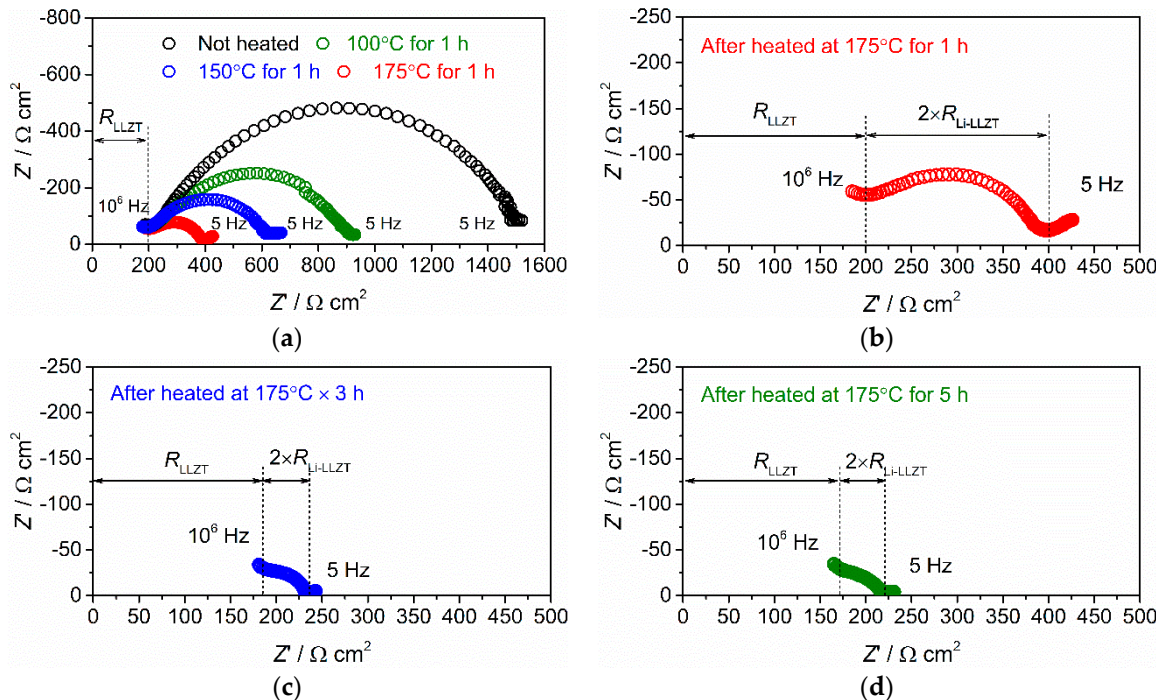


Figure 4. (a) Nyquist plots of AC impedance for Li/LLZT/Li symmetric cell at 27 °C before and after heat treatment at 100, 150, and 175 °C for one hour. Different Li/LLZT/Li cells heat treated at 175 °C for (b) one, (c) three, and (d) five hours.

In the frequency range of 5 Hz to 10^5 Hz, one semi-circle was clearly visible in the Li/LLZT/Li cell before and after applying heat treatment at different temperatures. This semi-circle was not observed in the Au/LLZT/Au cell shown in Figure 3a. At the high frequency range from 10^5 to 10^6 Hz, the plots almost overlap, suggesting that the data above 10^5 Hz are mainly attributed to the ionic conducting property of LLZT pellet. The data below 10^5 Hz correspond to the charge-transfer characteristics at the interface between LLZT and the two Li metal electrodes, and the diameter of the semicircle below 10^5 Hz corresponds to $2 \times R_{\text{Li-LLZT}}$. As shown in Figure 4a, $R_{\text{Li-LLZT}}$ decreased gradually as the heat treatment temperature increased. Before applying heat treatment, $R_{\text{Li-LLZT}}$ at 27 °C was $650 \Omega \text{ cm}^2$ and decreased to $350 \Omega \text{ cm}^2$, $200 \Omega \text{ cm}^2$, and $100 \Omega \text{ cm}^2$, after applying heat treatment at 100, 150, and 175 °C for one hour, respectively.

For further reduction of $R_{\text{Li-LLZT}}$, we investigated the influence of heat treatment time at 175 °C, which is only 5 °C lower than the melting point of Li. Nyquist plots of A/C impedance at 27 °C for Li/LLZT/Li cells heat-treated at 175 °C for one three, and five hours are shown in Figure 4b–d. $R_{\text{Li-LLZT}}$ was reduced further by increasing the heat treatment time, but both the cells heat treated at 175 °C for three and five hours showed the same $R_{\text{Li-LLZT}}$ of $25 \Omega \text{ cm}^2$ at 27 °C, indicating that the effect of heat treatment time on the reduction of $R_{\text{Li-LLZT}}$ was nearly saturated at three hours. We think that the reduction in $R_{\text{Li-LLZT}}$ obtained by optimizing the heat treatment condition resulted from improved wetting and contact between LLZT and Li.

Using the cell heat-treated at 175 °C for five hours, the temperature dependence of $R_{\text{Li-LLZT}}$ was investigated and the results are shown in Figure 5. The measurements were recorded in both heating and cooling processes at 27–100 °C. As shown in Figure 5a,b, the impedance data measured at a fixed

temperature in heating and cooling processes were nearly identical, suggesting that the resistances of LLZT, R_{LLZT} , and $R_{\text{Li-LLZT}}$ were hardly affected by temperatures below 100 °C.

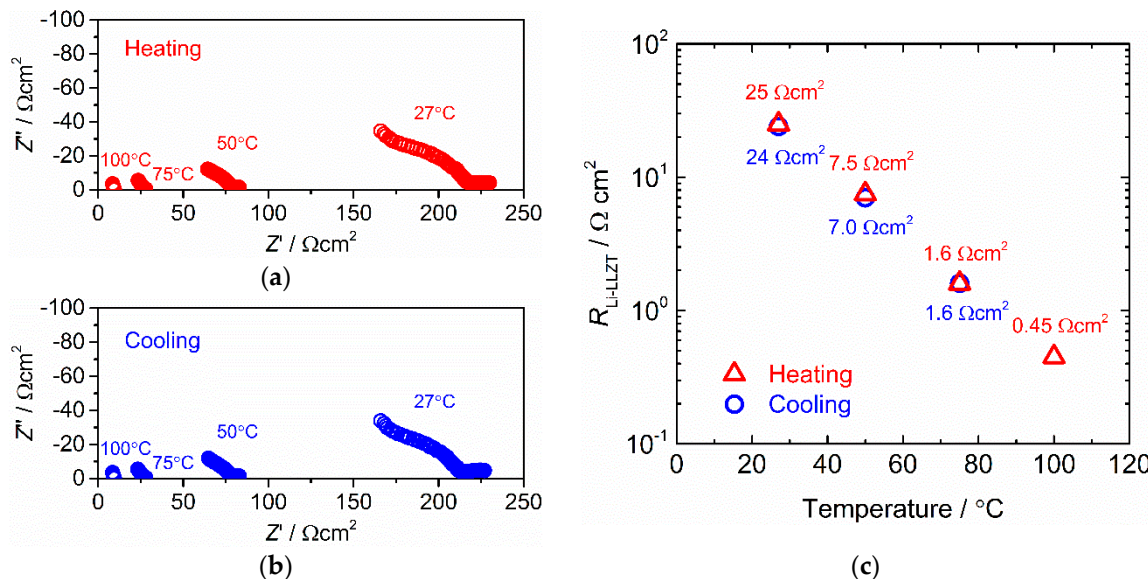


Figure 5. A/C impedance measured at different temperatures for Li/LLZT/Li symmetric cells after heat treatment at 175 °C for five hours: (a) during heating process from 27 to 100 °C and (b) cooling process from 100 to 27 °C. (c) Interfacial charge transfer resistance $R_{\text{Li-LLZT}}$ as a function of temperature.

3.3. Stability against Li Deposition and Dissolution Reaction at the Interface

Next, we discuss the stability against Li deposition and dissolution reaction at the interface between LLZT and Li. Figure 6 shows the results for galvanostatic cycling at 25 °C in Li/LLZT/Li symmetric cells with different $R_{\text{Li-LLZT}}$ (27 °C) of 100 and 25 $\Omega \text{ cm}^2$. In this work, “one cycle” is defined as the process of passing a current in both directions, and then resting for 600 s during each cycle. Cell voltage was determined as the product of current and cell resistance ($= R_{\text{LLZT}} + R_{\text{Li-LLZT}}$). In both cells, Ohmic behavior was observed at low current densities followed by deviation from Ohmic behavior at high current densities. Similar behavior has been confirmed in the literature [33,34,40–46]. Furthermore, the polarization was not symmetric against the current direction, which could have been caused by an irreversibility in Li deposition and dissolution reaction at each interface between LLZT and Li in a symmetric cell [43,46]. The cell with lower $R_{\text{Li-LLZT}}$ (Figure 6b) shows lesser polarization than the cell with higher $R_{\text{Li-LLZT}}$ (Figure 6a) and maintained Ohmic behavior under higher current densities around 0.1 mA cm^{-2} . The cell voltage suddenly dropped to 0 V at 0.11 mA cm^{-2} for the cell with an $R_{\text{Li-LLZT}}$ of 100 $\Omega \text{ cm}^2$, whereas the voltage drop in the cell with a lower $R_{\text{Li-LLZT}}$ of 25 $\Omega \text{ cm}^2$ occurred at 0.36 mA cm^{-2} . This indicates that the short circuit occurred inside the cell and the reduction of $R_{\text{Li-LLZT}}$ had a positive effect on enhancing the tolerance against the short circuit. Reducing $R_{\text{Li-LLZT}}$ likely resulted in more uniform current density, thus the tolerance against the short circuit improved. We also performed galvanostatic cycling for the symmetric cell at 100 °C. Increasing temperature improved wetting and contact between Li and LLZT. The $R_{\text{Li-LLZT}}$ of the tested cell was 25 $\Omega \text{ cm}^2$ at 27 °C and decreased to 0.5 $\Omega \text{ cm}^2$ at 100 °C. As expected, the current density at which the short circuit occurred increased to 1.2 mA cm^{-2} (Figure S1).

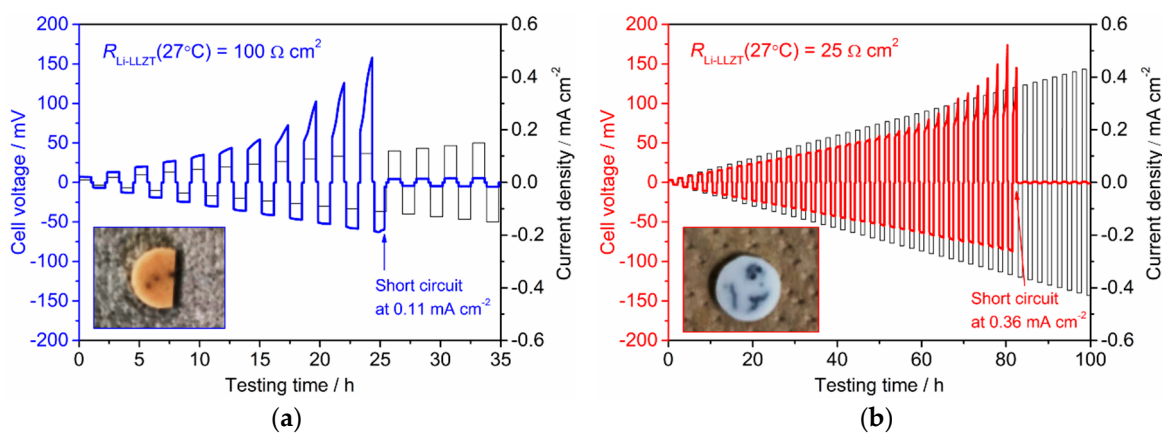


Figure 6. Galvanostatic cycling at 25 °C for Li/LLZT/Li cells with different $R_{\text{Li-LLZT}}$: (a) $R_{\text{Li-LLZT}}(27^\circ\text{C}) = 100 \Omega \text{ cm}^2$ and (b) $R_{\text{Li-LLZT}}(27^\circ\text{C}) = 25 \Omega \text{ cm}^2$. The inset in each graph is a photo of an LLZT pellet removed from each cell after a short circuit occurred.

The photos of the LLZT pellets removed from both cells after short circuits occurred are also shown in the insets of both graphs. Some black spots and cracks were clearly confirmed on the pellet surface. Moreover, some of the cracks penetrated along a thickness direction and reached the opposing pellet surface, indicating that the short circuit locally occurred around these cracks due to the propagation of Li dendrite into SE [33,47–49]. We also observed the microstructures of fractured cross sections of LLZT pellets using SEM and the results are shown in Figure 7. SEM observation was performed around the black spot. In Figure 7a, many fiber-like materials with submicron-sized diameters were confirmed between the LLZT grains in the pellet removed from the cell with $R_{\text{Li-LLZT}} = 100 \Omega \text{ cm}^2$. However, in Figure 7b, a whisker-like material two to three μm in diameter was confirmed to propagate into the pellet removed from the cell with $R_{\text{Li-LLZT}} = 25 \Omega \text{ cm}^2$. We think that these materials observed in LLZT pellets are Li dendrites that cause the short circuit during galvanostatic cycling test depicted in Figure 5.

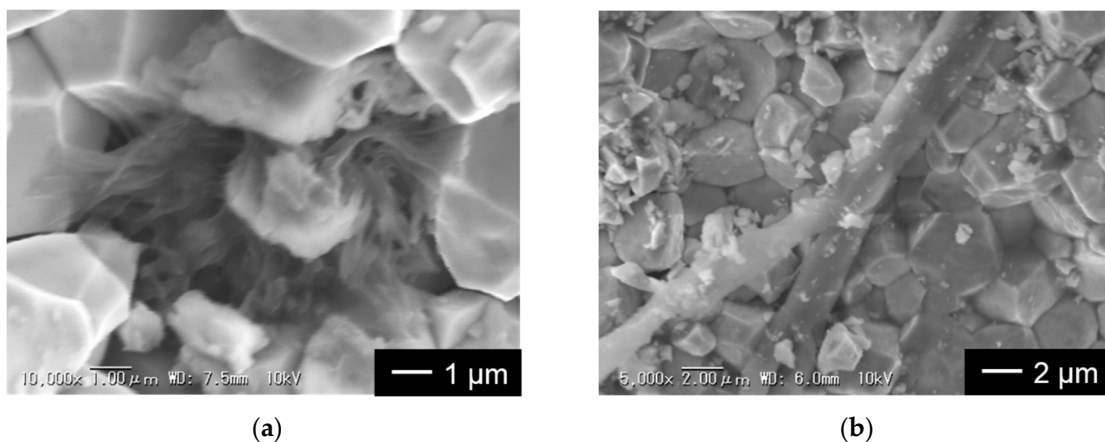


Figure 7. SEM images for cross sections of LLZT pellets removed from Li/LLZT/Li cells after a short circuit occurred: (a) $R_{\text{Li-LLZT}}(27^\circ\text{C}) = 100 \Omega \text{ cm}^2$ and (b) $R_{\text{Li-LLZT}}(27^\circ\text{C}) = 25 \Omega \text{ cm}^2$.

We fabricated other symmetric cells with $R_{\text{Li-LLZT}} = 25 \Omega \text{ cm}^2$ and their cycle stabilities were investigated at 25 °C and at current densities of 0.15 and 0.30 mA cm^{-2} for application times of one and two hours. The results are summarized in Figure 8. Notably, the measurements at these four different conditions were continuously performed in one specific cell. The cell was stably tested over 100 cycles without the occurrence of a short circuit at the conditions of 0.15 mA cm^{-2} for one hour,

0.15 mA cm^{-2} for two hours, and 0.30 mA cm^{-2} for one hour, whereas the polarization and deviation from Ohmic low become remarkable with increasing magnitude of current density and its application time. However, at 0.30 mA cm^{-2} for two hours, cell voltage increased abnormally in the first half cycle, and then a short circuit occurred during the second cycle. Under this condition, the cell could not be cycled stably.

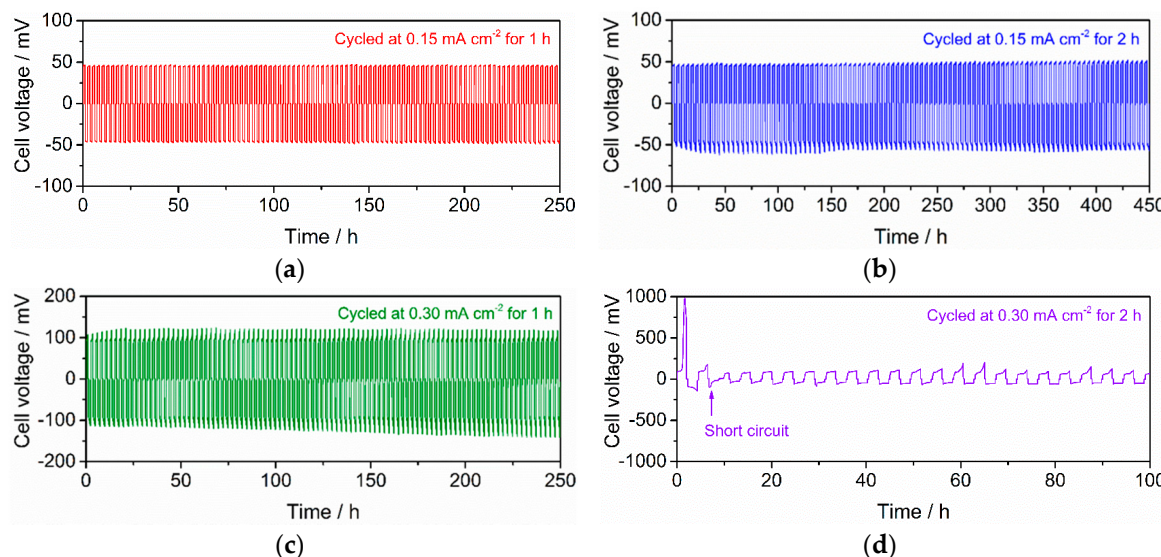


Figure 8. Galvanostatic cycling at 25°C for Li/LLZT/Li cell with $R_{\text{Li-LLZT}}(27^\circ\text{C}) = 25 \Omega \text{ cm}^2$: (a) cycled at 0.15 mA cm^{-2} for one hour, (b) cycled at 0.15 mA cm^{-2} for two hours, (c) cycled at 0.30 mA cm^{-2} for one hour, and (d) cycled at 0.30 mA cm^{-2} for two hours. The measurements were continuously recorded from (a) to (d).

Before and after each galvanostatic cycling under different conditions, we also checked the cell impedance at room temperature. The measurement results are shown in Figure 9. Before galvanostatic cycling, the cell resistance was around $230 \Omega \text{ cm}^2$. After being cycled at 0.15 mA cm^{-2} for one hour, 0.15 mA cm^{-2} for two hours, and 0.30 mA cm^{-2} for one hour, the cell demonstrated similar results and cell resistance ranging from 215 to $225 \Omega \text{ cm}^2$. This is consistent with the results for the stable galvanostatic cycling shown in Figure 8a–c. However, after being cycled at 0.30 mA cm^{-2} for two hours, the plot significantly deviated from the others and the cell resistance decreased to $65 \Omega \text{ cm}^2$.

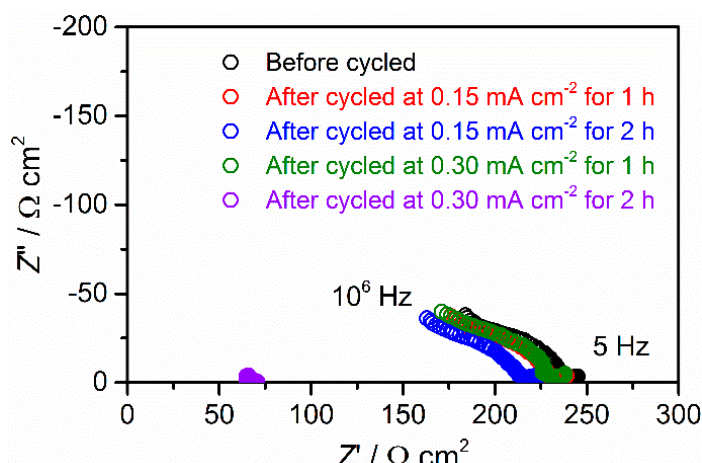


Figure 9. A/C impedance measured at 27°C for Li/LLZT/Li cell before and after galvanostatic cycling with different conditions described in the caption of Figure 8.

The conditions for the stable cycling of a symmetric cell were expected to be influenced not only by the magnitude of the current density but also by the capacity for Li deposition at the interface between LLZT and Li. Using the data for the first half cycle in Figure 8c,d, the change in cell voltage at 25 °C and 0.30 mA cm⁻² are plotted as a function of area specific capacity for Li deposition (Figure 10). The plots of the cell voltage tested at 0.30 mA cm⁻² for one and two hours nearly overlapped at the capacity for Li deposition below 0.30 mAh cm⁻² and an abnormal increase in cell voltage was caused at a capacity above 0.35 mAh cm⁻². Similar behavior was confirmed when the cell was cycled at smaller current density of 0.15 mA cm⁻². As shown in Figure 8a,b, the cell was stably cycled at 0.15 mA cm⁻² for one and two hours, but a short circuit occurred at 0.15 mA cm⁻² for three hours (Figure S2). The abnormal increase in cell voltage was also confirmed at the capacity for Li deposition above 0.30 mAh cm⁻² (Figure S3). Although our measurement conditions in this work were limited, the threshold of the area for specific Li deposition capacity for stable was roughly expected to be around 0.30 mAh cm⁻². When we used the LLZT prepared in this work, the $R_{\text{Li-LLZT}}$ at room temperature decreased to 20–30 Ω cm², and the current density for galvanostatic cycling was set below 0.30 mA cm⁻².

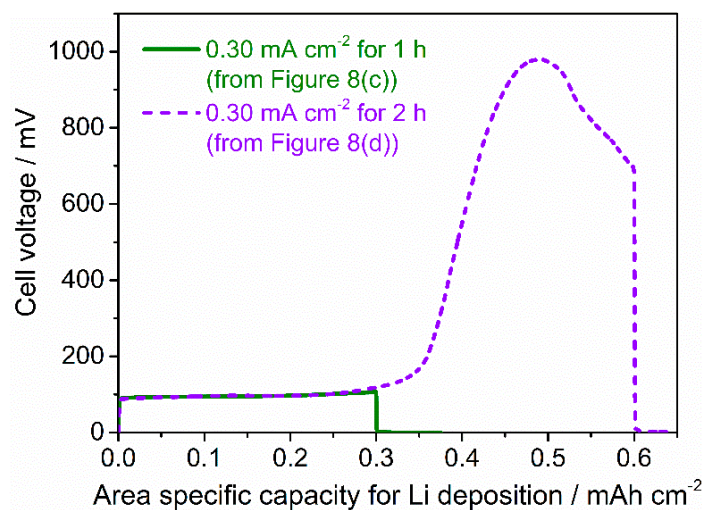


Figure 10. Cell voltage at 25 °C and 0.30 mA cm⁻² for one or two hours in Li/LLZT/Li cell with $R_{\text{Li-LLZT}}(27^{\circ}\text{C}) = 25 \Omega \text{ cm}^2$, as a function of area specific capacity for Li deposition. The plotted data were calculated from the data from the first cycle in Figure 8c,d.

Together with further examination of the propagation mechanism of Li dendrite into garnet-type SE, both the critical current density at which the short circuit occurs and the threshold in the capacity for Li deposition for stable cycling must be enhanced further to realize a solid-state battery with a garnet-type oxide SE and Li metal anode. We believe that this could be achieved by reducing the interfacial charge-transfer resistance further and by structural improvement of the garnet-type SE by decreasing the porosity [34,47,48], controlling grain size [41,44], and modifying the grain boundary [45,50].

4. Conclusions

We investigated the influence of heating temperature and time on the interfacial resistance between LLZT and a Li metal electrode using a Li/LLZT/Li symmetric cell. In addition, the effect of the interfacial charge-transfer resistance $R_{\text{Li-LLZT}}$ on the stability of Li deposition and dissolution was investigated using a galvanostatic cycling test. The lowest $R_{\text{Li-LLZT}}$ of 25 Ω cm² at room temperature was obtained by heating at 175 °C for three to five hours after contacting LLZT with Li. We confirmed that reducing interfacial resistance is effective for enhancing the current density at which the short circuit occurs by propagating the Li dendrite into LLZT. The conditions for stable cycling of a symmetric

cell are influenced not only by the magnitude of the current density but also by the capacity for Li deposition at the interface between LLZT and Li.

Supplementary Materials: The following are available online at <http://www.mdpi.com/2313-0105/4/2/26/s1>, Figure S1: Galvanostatic cycling at 100 °C for Li/LLZT/Li cell with $R_{\text{Li-LLZT}} = 25 \text{ cm}^2$ at 27 °C and 0.5 cm² at 100 °C, Figure S2: Galvanostatic cycling at 25 °C for Li/LLZT/Li cell with $R_{\text{Li-LLZT}}$ (27 °C) = 28 cm² tested at 0.15 mA cm⁻² for 3 h, Figure S3: Cell voltage at 25 °C and 0.15 mA cm⁻² for 1, 2 and 3 h in Li/LLZT/Li cells as a function of area specific capacity for Li deposition.

Author Contributions: R.I., S.Y., H.H., M.S. conceived, designed, and executed the experiments. All authors were involved in the analysis of the results. R.I. wrote the manuscript. All authors were involved in the discussion of the results and manuscript.

Acknowledgments: This work was partly supported by JSPS KAKENHI grant numbers 16K06218 and 16KK0127 from the Japan Society for the Promotion of Science (JSPS) and Research Foundation for the Electro-technology of Chubu (R-28241).

Conflicts of Interest: The authors declare no conflict of interest.

References

1. Armand, M.; Tarascon, J.M. Building better batteries. *Nature* **2008**, *451*, 652–657. [[CrossRef](#)] [[PubMed](#)]
2. Scrosati, B.; Garche, J. Lithium batteries: Status, prospects and future. *J. Power Sources* **2010**, *195*, 2419–2430. [[CrossRef](#)]
3. Goodenough, J.B.; Kim, Y. Challenges for rechargeable batteries. *J. Power Sources* **2011**, *196*, 6688–6694. [[CrossRef](#)]
4. Fergus, J.W. Ceramic and polymeric solid electrolytes for lithium-ion batteries. *J. Power Sources* **2010**, *195*, 4554–4569. [[CrossRef](#)]
5. Takada, K. Progress and prospective of solid-state lithium batteries. *Acta Mater.* **2012**, *61*, 759–770. [[CrossRef](#)]
6. Tatsumisago, M.; Nagao, M.; Hayashi, A. Recent development of sulfide solid electrolytes and interfacial modification for all-solid-state rechargeable lithium batteries. *J. Asian Ceram. Soc.* **2013**, *1*, 117–125. [[CrossRef](#)]
7. Knauth, P. Inorganic solid Li ion conductors: An overview. *Solid State Ion.* **2009**, *180*, 911–916. [[CrossRef](#)]
8. Ren, Y.; Chen, K.; Chen, R.; Liu, T.; Zhang, Y.; Nan, C.-W. Oxide electrolytes for lithium batteries. *J. Am. Ceram. Soc.* **2015**, *98*, 3603–3623. [[CrossRef](#)]
9. Murugan, R.; Thangadurai, V.; Weppner, W. Fast lithium ion conduction in garnet-type $\text{Li}_7\text{La}_3\text{Zr}_2\text{O}_{12}$. *Angew. Chem. Int. Ed.* **2007**, *46*, 7778–7781. [[CrossRef](#)] [[PubMed](#)]
10. Awaka, J.; Takashima, A.; Kataoka, K.; Kijima, N.; Idemoto, Y.; Akimoto, J. Crystal structure of fast lithium-ion-conducting cubic $\text{Li}_7\text{La}_3\text{Zr}_2\text{O}_{12}$. *Chem. Lett.* **2011**, *40*, 60–62. [[CrossRef](#)]
11. Awaka, J.; Kijima, N.; Hayakawa, H.; Akimoto, J. Synthesis and structure analysis of tetragonal $\text{Li}_7\text{La}_3\text{Zr}_2\text{O}_{12}$ with the garnet-related type structure. *J. Solid State Chem.* **2009**, *182*, 2046–2052. [[CrossRef](#)]
12. Geiger, C.A.; Alekseev, E.; Lazic, B.; Fisch, M.; Armbruster, T.; Langner, R.; Fechtelkord, M.; Kim, N.; Pettke, T.; Weppner, W. Crystal chemistry and stability of “ $\text{Li}_7\text{La}_3\text{Zr}_2\text{O}_{12}$ ” garnet: A fast lithium-ion conductor. *Inorg. Chem.* **2011**, *50*, 1089–1097. [[CrossRef](#)] [[PubMed](#)]
13. Ohta, S.; Kobayashi, T.; Asaoka, T. High lithium ionic conductivity in the garnet-type oxide $\text{Li}_{7-x}\text{La}_3(\text{Zr}_{2-x}, \text{Nb}_x)\text{O}_{12}$ ($X = 0\text{--}2$). *J. Power Sources* **2011**, *196*, 3342–3345. [[CrossRef](#)]
14. Kihira, Y.; Ohta, S.; Imagawa, H.; Asaoka, T. Effect of simultaneous substitution of alkali earth metals and Nb in $\text{Li}_7\text{La}_3\text{Zr}_2\text{O}_{12}$ on lithium-ion conductivity. *ECS Electrochem. Lett.* **2013**, *2*, A56–A59. [[CrossRef](#)]
15. Li, Y.; Han, J.-T.; Wang, C.-A.; Xie, H.; Goodenough, J.B. Optimizing Li^+ conductivity in a garnet framework. *J. Mater. Chem.* **2012**, *22*, 15357–15361. [[CrossRef](#)]
16. Buschmann, H.; Berendts, S.; Mogwitz, B.; Janek, J. Lithium metal electrode kinetics and ionic conductivity of the solid lithium ion conductors “ $\text{Li}_7\text{La}_3\text{Zr}_2\text{O}_{12}$ ” and $\text{Li}_{7-x}\text{La}_3\text{Zr}_{2-x}\text{Ta}_x\text{O}_{12}$ with garnet-type structure. *J. Power Sources* **2012**, *206*, 236–244. [[CrossRef](#)]
17. Logéat, A.; Köhler, T.; Eisele, U.; Stiaszny, B.; Harzer, A.; Tovar, M.; Senyshyn, A.; Ehrenberg, H.; Kozinsky, B. From order to disorder: The structure of lithium-conducting garnets $\text{Li}_{7-x}\text{La}_3\text{Ta}_x\text{Zr}_{2-x}\text{O}_{12}$ ($x = 0\text{--}2$). *Solid State Ion.* **2012**, *206*, 33–38. [[CrossRef](#)]
18. Wang, Y.; Wei, L. High ionic conductivity lithium garnet oxides of $\text{Li}_{7-x}\text{La}_3\text{Zr}_{2-x}\text{Ta}_x\text{O}_{12}$ compositions. *Electrochim. Solid State Lett.* **2012**, *15*, A68–A71. [[CrossRef](#)]

19. Thompson, T.; Sharafi, A.; Johannes, M.D.; Huq, A.; Allen, J.L.; Wolfenstine, J.; Sakamoto, J. Tale of two sites: On defining the carrier concentration in garnet-based ionic conductors for advanced Li batteries. *Adv. Energy Mater.* **2015**, *5*, 1500096. [[CrossRef](#)]
20. Thompson, T.; Wolfenstine, J.; Allen, J.L.; Johannes, M.; Huq, A.; Davida, I.N.; Sakamoto, J. Tetragonal vs. cubic phase stability in Al-free Ta doped $\text{Li}_7\text{La}_3\text{Zr}_2\text{O}_{12}$ (LLZO). *J. Mater. Chem. A* **2014**, *2*, 13431–13436. [[CrossRef](#)]
21. Inada, R.; Kusakabe, K.; Tanaka, T.; Kudo, S.; Sakurai, Y. Synthesis and properties of Al-free $\text{Li}_{7-x}\text{La}_3\text{Zr}_{2-x}\text{Ta}_x\text{O}_{12}$ garnet related oxides. *Solid State Ion.* **2014**, *262*, 568–572. [[CrossRef](#)]
22. Inada, R.; Yasuda, S.; Tojo, T.; Sakurai, Y. Development of lithium-stuffed garnet-type oxide solid electrolytes with high ionic conductivity for application to all-solid-state batteries. *Front. Energy Res.* **2016**, *4*, 28. [[CrossRef](#)]
23. Ren, Y.; Deng, H.; Chen, R.; Shen, Y.; Lin, Y.; Nan, C.-W. Effects of Li source on microstructure and ionic conductivity of Al-contained $\text{Li}_{6.75}\text{La}_3\text{Zr}_{1.75}\text{Ta}_{0.25}\text{O}_{12}$ ceramics. *J. Eur. Ceram. Soc.* **2015**, *35*, 561–572. [[CrossRef](#)]
24. Dhivya, L.; Janani, N.; Palanivel, B.; Murugan, R. Li⁺ transport properties of W substituted $\text{Li}_7\text{La}_3\text{Zr}_2\text{O}_{12}$ cubic lithium garnets. *AIP Adv.* **2013**, *3*, 082115. [[CrossRef](#)]
25. Li, Y.; Wang, Z.; Cao, Y.; Du, F.; Chen, C.; Cui, Z.; Guo, X. W-doped $\text{Li}_7\text{La}_3\text{Zr}_2\text{O}_{12}$ ceramic electrolytes for solid state Li-ion batteries. *Electrochim. Acta* **2015**, *180*, 37–42. [[CrossRef](#)]
26. Bottke, P.; Rettenwander, D.; Schmidt, W.; Amthauer, G.; Wilkening, M. Ion dynamics in solid electrolytes: NMR reveals the elementary steps of Li⁺ hopping in the garnet $\text{Li}_{6.5}\text{La}_3\text{Zr}_{1.75}\text{Mo}_{0.25}\text{O}_{12}$. *Chem. Mater.* **2015**, *27*, 6571–6582. [[CrossRef](#)]
27. Ohta, S.; Komagata, S.; Seki, J.; Saeki, T.; Morishita, S.; Asaoka, T. All solid-state lithium ion battery using garnet-type oxide and Li_3BO_3 solid electrolytes fabricated by screen-printing. *J. Power Sources* **2013**, *238*, 53–56. [[CrossRef](#)]
28. Ohta, S.; Seki, J.; Yagi, Y.; Kihira, Y.; Tani, T.; Asaoka, T. Co-sinterable lithium garnet-type oxide electrolyte with cathode for all-solid-state lithium ion battery. *J. Power Sources* **2014**, *265*, 40–44. [[CrossRef](#)]
29. Nemori, H.; Matsuda, Y.; Mitsuoka, S.; Matsui, M.; Yamamoto, O.; Takeda, Y.; Imanishi, N. Stability of garnet-type solid electrolyte $\text{Li}_x\text{La}_3\text{A}_{2-y}\text{B}_y\text{O}_{12}$ (A = Nb or Ta, B = Sc or Zr). *Solid State Ion.* **2015**, *282*, 7–12. [[CrossRef](#)]
30. Kim, Y.; Yoo, A.; Schmidt, R.; Sharafi, A.; Lee, H.; Wolfenstine, J.; Sakamoto, J. Electrochemical Stability of $\text{Li}_{6.5}\text{La}_3\text{Zr}_{1.5}\text{M}_{0.5}\text{O}_{12}$ (M = Nb or Ta) against Metallic Lithium. *Front. Energy Res.* **2016**, *4*, 20. [[CrossRef](#)]
31. Xie, H.; Park, K.-S.; Song, J.; Goodenough, J.B. Reversible lithium insertion in the garnet framework of $\text{Li}_3\text{Nd}_3\text{W}_2\text{O}_{12}$. *Electrochem. Commun.* **2012**, *19*, 135–137. [[CrossRef](#)]
32. Hofstetter, K.; Samson, A.J.; Narayanan, S.; Thangadurai, V. Present understanding of the stability of Li-stuffed garnets with moisture, carbon dioxide, and metallic lithium. *J. Power Sources* **2018**, *390*, 297–312. [[CrossRef](#)]
33. Sharafi, A.; Meyer, H.M.; Nanda, J.; Wolfenstine, J.; Sakamoto, J. Characterizing the Li– $\text{Li}_7\text{La}_3\text{Zr}_2\text{O}_{12}$ interface stability and kinetics as a function of temperature and current density. *J. Power Sources* **2016**, *302*, 135–139. [[CrossRef](#)]
34. Basappa, R.H.; Ito, T.; Yamada, H. Contact between garnet-type solid electrolyte and lithium metal anode: Influence on charge transfer resistance and short circuit prevention. *J. Electrochem. Soc.* **2017**, *164*, A666–A671. [[CrossRef](#)]
35. Tsai, C.-L.; Roddatis, V.; Chandran, C.V.; Ma, Q.; Uhlenbruck, S.; Bram, M.; Heitjans, P.; Guillou, O. Li₇La₃Zr₂O₁₂ interface modification for Li dendrite prevention. *ACS Appl. Mater. Interfaces* **2016**, *8*, 10617–10626. [[CrossRef](#)] [[PubMed](#)]
36. Luo, W.; Gong, Y.; Zhu, Y.; Fu, K.K.; Dai, J.; Lacey, S.D.; Wang, C.; Liu, B.; Han, X.; Mo, Y.; et al. Transition from superlithiophobicity to superlithiophilicity of garnet solid-state electrolyte. *J. Am. Chem. Soc.* **2016**, *138*, 12258–12262. [[CrossRef](#)] [[PubMed](#)]
37. Luo, W.; Gong, Y.; Zhu, Y.; Li, Y.; Yao, Y.; Zhang, Y.; Fu, K.; Pastel, G.; Lin, C.-F.; Mo, Y.; et al. Reducing interfacial resistance between garnet-structured solid-state electrolyte and Li-metal Anode by a germanium layer. *Adv. Mater.* **2017**, *29*, 1606042. [[CrossRef](#)] [[PubMed](#)]
38. Han, X.; Gong, Y.; Fu, K.; He, X.; Hitz, G.T.; Dai, J.; Pearse, A.; Liu, B.; Wang, H.; Rublo, G.; et al. Negating interfacial impedance in garnet-based solid-state Li metal batteries. *Nat. Mater.* **2017**, *16*, 572–579. [[CrossRef](#)] [[PubMed](#)]

39. Wang, C.; Gong, Y.; Liu, B.; Fu, K.; Yao, Y.; Hitz, E.; Li, Y.; Dai, J.; Xu, S.; Luo, W.; et al. Conformal, nanoscale ZnO surface modification of garnet based solid-state electrolyte for lithium metal anodes. *Nano Lett.* **2017**, *17*, 565–571. [[CrossRef](#)] [[PubMed](#)]
40. Sharafi, A.; Kazyak, E.; Davis, A.L.; Yu, S.; Thompson, T.; Siegel, D.J.; Dasgupta, N.P.; Sakamoto, J. Surface chemistry mechanism of ultra-low interfacial resistance in the solid-state electrolyte $\text{Li}_7\text{La}_3\text{Zr}_2\text{O}_{12}$. *Chem. Mater.* **2017**, *29*, 7961–7968. [[CrossRef](#)]
41. Sharafi, A.; Meyer, H.M.; Nanda, J.; Wolfenstine, J.; Sakamoto, J. Controlling and correlating the effect of grain size with the mechanical and electrochemical properties of $\text{Li}_7\text{La}_3\text{Zr}_2\text{O}_{12}$ solid-state electrolyte. *J. Mater. Chem. A* **2017**, *5*, 21491–21504. [[CrossRef](#)]
42. Wang, M.; Sakamoto, J. Correlating the interface resistance and surface adhesion of the Li metal solid electrolyte interface. *J. Power Sources* **2018**, *377*, 7–11. [[CrossRef](#)]
43. Yonemoto, F.; Nishimura, A.; Motoyama, M.; Tsuchimine, N.; Kobayashi, S.; Iriyama, Y. Temperature effects on cycling stability of Li plating/stripping on Ta-doped $\text{Li}_7\text{La}_3\text{Zr}_2\text{O}_{12}$. *J. Power Sources* **2017**, *343*, 207–215. [[CrossRef](#)]
44. Yamada, H.; Ito, T.; Rajendra, H.B. Sintering mechanisms of high-performance garnet-type solid electrolyte densified by spark plasma sintering. *Electrochim. Acta* **2016**, *222*, 648–656. [[CrossRef](#)]
45. Basappa, R.H.; Ito, T.; Morimura, T.; Bekarevich, R.; Mitsuishi, K.; Yamada, H. Grain boundary modification to suppress lithium penetration through garnet-type solid electrolyte. *J. Power Sources* **2017**, *363*, 145–152. [[CrossRef](#)]
46. Koshikawa, H.; Matsuda, S.; Kamiya, K.; Miyayama, M.; Kubo, Y.; Uosaki, K.; Hashimoto, K.; Nakanishi, S. Dynamic changes in charge-transfer resistance at Li metal/ $\text{Li}_7\text{La}_3\text{Zr}_2\text{O}_{12}$ interfaces during electrochemical Li dissolution/deposition cycles. *J. Power Sources* **2018**, *376*, 147–151. [[CrossRef](#)]
47. Ren, Y.; Shen, Y.; Lin, Y.; Nan, C.-W. Direct observation of lithium dendrites inside garnet-type lithium-ion solid electrolyte. *Electrochem. Commun.* **2015**, *57*, 27–30. [[CrossRef](#)]
48. Suzuki, Y.; Kami, K.; Watanabe, K.; Watanabe, A.; Saito, N.; Ohnishi, T.; Takada, K.; Sudo, R.; Imanishi, N. Transparent cubic garnet-type solid electrolyte of Al_2O_3 -doped $\text{Li}_7\text{La}_3\text{Zr}_2\text{O}_{12}$. *Solid State Ion.* **2015**, *278*, 172–176. [[CrossRef](#)]
49. Cheng, E.J.; Sharafi, A.; Sakamoto, J. Intergranular Li metal propagation through polycrystalline $\text{Li}_{6.25}\text{Al}_{0.25}\text{La}_3\text{Zr}_2\text{O}_{12}$ ceramic electrolyte. *Electrochim. Acta* **2017**, *223*, 85–91. [[CrossRef](#)]
50. Xu, B.; Li, W.; Duan, H.; Wang, H.; Guo, Y.; Li, H.; Liu, H. Li_3PO_4 -added garnet-type $\text{Li}_{6.5}\text{La}_3\text{Zr}_{1.5}\text{Ta}_{0.5}\text{O}_{12}$ for Li-dendrite suppression. *J. Power Sources* **2017**, *354*, 68–73. [[CrossRef](#)]



© 2018 by the authors. Licensee MDPI, Basel, Switzerland. This article is an open access article distributed under the terms and conditions of the Creative Commons Attribution (CC BY) license (<http://creativecommons.org/licenses/by/4.0/>).